

A persistent homology based prior for the potential coefficient reconstruction problem in an elliptic equation

Zhiliang Deng^{* 1}, Haiyang Liu¹, Xiaofei Guan², Zhiyuan Wang², and Xiaomei Yang³

¹University of Electronic Science and Technology of China

²Tongji University

³Southwest Jiaotong University

August 5, 2025

Abstract

This paper addresses the reconstruction of a potential coefficient in an elliptic problem from distributed observations within the Bayesian framework. In such problems, the selection of an appropriate prior distribution is crucial, particularly when the function to be inferred exhibits sharp discontinuities, as traditional Gaussian priors often prove inadequate. To tackle this challenge, we develop a persistent homology based prior (PH), a new prior constructed using persistent homology. The proposed prior utilizes persistent pairs to characterize and record the topological variations of the functions under reconstruction, thereby encoding prior information about the structure and discontinuities of the function. The PH prior, however, only exists in a discretized formulation, which leads to the absence of a well-defined posterior measure in function spaces. To resolve this issue, we propose a PH-Gaussian hybrid prior, where the PH component detects sharp discontinuities in the function, while the Gaussian distribution acts as a reference measure, ensuring a well-defined posterior measure in the function space. The proposed PH prior exhibits properties analogous to those of the classical TV prior, while providing enhanced flexibility and a wider range of applications. This positions the PH prior as a natural generalization of the TV prior framework.

Keywords: Inverse potential problems, topological prior, Bayesian approach, persistent homology, TV prior

^{*}dengzhl@uestc.edu.cn

1 Introduction

The inverse potential problem we study in the paper is governed by the elliptic equation

$$\begin{cases} -\Delta u + qu = f & \text{in } \Omega, \\ u = 0 & \text{on } \partial\Omega, \end{cases} \quad (1)$$

where $\Omega \subset \mathbb{R}^s$ ($s = 1, 2$) is a bounded open domain, and the function f is the known source term. The potential q belongs to the admissible set K defined as

$$K = \{q \in L^\infty(\Omega) : c_0 \leq q(x) \leq c_1 \text{ a.e. in } \Omega\}, \quad (2)$$

with $0 \leq c_0 < c_1 < \infty$. We collect the observational data of the solution $u(x)$ to (1) on Ω by

$$u^\eta(x) = u(x) + \eta(x), \quad x \in \Omega, \quad (3)$$

where η denotes the measurement noise. The inverse potential problem aims to estimate the potential function q from the noisy observation u^η . This issue has potential relevance to various applied fields. M. Choulli's work [11] briefly notes its possible connections to dynamic elastography, microwave imaging, and acousto-optic imaging, though without detailed case analysis. In [1], G. Bal and G. Uhlmann discussed the reconstruction of an absorption coefficient in the photoacoustic tomography problem by the internal observation data in a scattering medium. In some real-world cases, the inverse potential problem is also inherently linked to time-dependent phenomena, e.g., the reconstruction of the radiativity coefficient in heat equation [1, 29, 39, 43, 45] and the reconstruction of the potential in Schrödinger equation [3, 4]. Due to their wide-ranging real-world applications, inverse potential problems have garnered significant attention from researchers.

Several theoretical perspectives associated with this problem have been studied by some authors. For example, [1, 29] systematically investigate the uniqueness and conditional stability of the solution. In addition, [11] establishes both Lipschitz and Hölder stability estimates. These works provide sufficient conditions under which the solution is uniquely determined and remains stable with respect to perturbations in the data. For convergence analysis and uncertainty quantification, R. Nickl [37] derived posterior contraction rates and proved a Bernstein–von Mises theorem, ensuring consistency of the Bayesian posterior and providing rigorous uncertainty quantification. In [38], the convergence rate of the maximum a posteriori (MAP) estimator within the same Bayesian framework is further investigated. In [30], B. Jin et al examine the case where observational data is collected on uniform or quasi-uniform grids, deriving explicit error bounds for the resulting estimates from the viewpoint of regularization theory.

From the perspective of numerical methods, the core challenge lies in the ill-posed nature of inverse problems, which severely complicates the construction of accurate and stable numerical approximations. Ill-posedness—manifested through extreme sensitivity to data noise and potential non-uniqueness of solutions—necessitates the development of specialized regularization strategies and robust computational algorithms to ensure reliable and interpretable results. Extensive research has been devoted to addressing these challenges, leading to the emergence of two dominant methodological paradigms: (1) regularization-based approaches, such as Tikhonov regularization [5, 20, 21, 28], and

(2) statistical inference techniques, particularly those rooted in the Bayesian framework [13, 33–35, 41, 42].

Tikhonov regularization, in particular, has seen widespread application in solving inverse potential problems. It enhances the stability of numerical solutions by incorporating prior information to regularize ill-posed models [20, 29], and has demonstrated substantial success in dealing with noisy and incomplete data.

In contrast, the Bayesian approach offers a flexible and probabilistically grounded framework for incorporating uncertainty in both data and model parameters. It yields posterior distributions that quantify uncertainty and enable probabilistic inference. Notably, the theoretical well-posedness of Bayesian inversion—established in foundational works such as [13, 41]—has made it a central methodology in the study of inverse problems. Recent advances by J. Latz [34, 35] further extend these results under minimal assumptions on likelihoods and priors, and examine well-posedness across multiple probabilistic metrics, including the Hellinger distance, total variation distance, weak convergence, and the Wasserstein metric. These theoretical developments have fueled the practical success of Bayesian methods in a wide range of inverse problems. In inverse scattering, for instance, Bayesian techniques have proven effective for inferring posterior distributions of obstacle shapes [8, 10, 36] and refractive indices [22, 25, 32] from scattered field measurements. Similarly, Bayesian inversion has been extensively applied to reconstruct conductivity parameters in elliptic PDEs [6, 13, 23, 41].

A key element in Bayesian inversion is the specification of the prior distribution, which encodes prior beliefs or structural assumptions about the unknowns and plays a role analogous to that of the regularizer in classical methods. Considerable effort has been dedicated to designing appropriate priors. For example, priors based on Markov random fields offer a rich modeling framework [2, 27], while [37] introduces a wavelet-based prior for the reconstruction of potential coefficients. To address inverse problems with less regular parameters, [44] proposes an l_1 -type prior that includes both the TV prior and the Besov space $B_{1,1}^s$ prior. In [46], a hybrid TV-Gaussian prior is developed to better capture sharp discontinuities in the target function. The incorporation of geometric information into the prior is another fruitful line of research, especially in problems involving geometric reconstructions. In a series of works [9, 10], A. Carpio and collaborators propose a novel prior construction strategy grounded in the topological energy landscape of objective functions, which they successfully apply to inverse scattering and wave equation parameter estimation. Similarly, [26] introduces a geometry-informed prior formulation, where prior assumptions are guided by the structural characteristics of the unknown domain.

In this paper, we provide a survey of the application of the Bayesian method to the inverse potential problem. Our main contribution is the proposal of a new prior based on the topological tool of persistent homology. This prior aims to constrain the topological variation of the unknown, thereby imparting a degree of smoothness. It can be demonstrated that the new prior serves a similar role to that of the classical TV prior. It should be noted that the proposed PH based prior differs from that in [9, 10]. In [9, 10], the primary focus is on exploiting the topological energies of associated objective function. In contrast, our method emphasizes the topological structure inherent in the unknown functions. These topological features are encoded in the so-called persistence diagrams, which allow us to extract and analyze the latent shape information. This new prior introduces a fresh viewpoint for understanding the unknown functions. We present several numerical

examples to illustrate the effectiveness of the proposed prior. Through comprehensive numerical experiments, we demonstrate that our approach achieves substantially better performance than Gaussian priors for non-smooth function estimation, particularly in cases involving abrupt changes (e.g., sharp jumps or step discontinuities). Furthermore, in line with the theoretical insights from [47], the PH-based prior exhibits behavior similar to that of TV-based priors [46], as evidenced by the numerical results. We emphasize the key distinctions: (a) The PH-based prior is defined on a general topological space that preserves richer topological information, substantially expanding its potential applications across multiple domains; (b) The PH-based prior enables more robust results with greater ease, owing to its increased number of adjustable parameters compared to the TV-based prior. These characteristics formally extend the TV prior framework while preserving its core regularization properties.

This paper is organized as follows: In Section 2 we present the necessary background on persistent homology; In Section 3 we discuss the Bayesian approach with PH-Gaussian hybrid prior; In Section 4, we introduce the pCN sampling algorithm; In Section 5 we present our numerical examples and results. Lastly in Section 6 we give some conclusions.

2 Persistent homology

This section introduces necessary background knowledge on persistence diagram and persistent homology which forms a concrete basement for our prior. For more details one can refer to [47, 48].

We consider a space (object) X that varies as a function of a parameter r . When the parameter is fixed at a specific value \tilde{r} , homology groups characterize the essential topological features of $X(\tilde{r})$, providing a means to classify k -dimensional holes in $X(\tilde{r})$. Persistent homology captures the changes in the shape of this object as the parameter r varies. Actually, when the parameter r changes until a certain critical value is reached, the topology of the object also undergoes changes. We can observe the birth of new k -dimensional holes and the death of existing ones. The birth time $r = b$ of a k -dimensional hole is recorded, as is the death time $r = d$. The persistence of this k -dimensional hole is denoted as $d - b$. This dynamic process can be illustrated by what is known as a filtration process.

For simplicity, we assume that the object X is a simplicial complex that is homeomorphic to a specific geometric object, typically its triangulation X . We suppose that X has $m + 1$ vertices $\{p_0, \dots, p_m\} \subset \mathbb{R}^d$. A simplicial complex is a set composed of basic cells, including points, line segments, triangles, and their n -dimensional counterparts, constructed from the subsets of $\{p_0, \dots, p_m\}$. These cells, referred to as simplices, are organized in a way that respects the combinatorial structure of the complex, where each cell is defined by its vertices and is associated with lower-dimensional cells that form its boundary. Specifically, a k -dimensional simplex σ , or k -simplex, $k \leq m$, is the set of convex combinations of $k + 1$ affinely independent points $\{p_0, p_1, \dots, p_k\}$, i.e.,

$$\sigma = \left\{ \sum_{i=0}^k \lambda_i p_i \mid \sum_{i=0}^k \lambda_i = 1 \text{ and } \lambda_i \geq 0 \right\}. \quad (4)$$

The points p_0, p_1, \dots, p_k are called the vertices of σ and the number k the dimension of σ . We denote the simplex as $\langle p_0, \dots, p_k \rangle$, i.e., $\sigma = \langle p_0, \dots, p_k \rangle$. Any simplex spanned

by a subset of $\{p_0, p_1, \dots, p_k\}$ is called a face of σ . If τ is a face of σ , then σ is a coface of τ . With the concept of simplices, we can define the simplicial complex X in \mathbb{R}^d as a (finite) collection of simplices such that:

- i. any face of a simplex of X is a simplex of X ;
- ii. the intersection of any two simplices of X is either empty or a common face of both.

We denote the set generated by k -simplices of X over the binary field \mathbb{Z}_2 as $C_k = C_k(X)$. It consists of all k -chains as

$$\mathbf{c} = \sum_j \gamma_j \sigma_j, \quad (5)$$

where γ_j are 0 or 1 and σ_j are k -simplices in X . The addition over \mathbb{Z}_2 for two k -chains is defined by $\mathbf{c} + \tilde{\mathbf{c}} = \sum_j (\gamma_j + \tilde{\gamma}_j) \sigma_j$, where $\mathbf{c} = \sum_j \gamma_j \sigma_j$ and $\tilde{\mathbf{c}} = \sum_j \tilde{\gamma}_j \sigma_j$. The k -chains in C_k form a group under this addition, which we denote as $(C_k, +)$ and refer to as the group of k -chains.

Different types of chains in X are distinguished by homology group, which is defined by virtue of the quotient group. To establish this, we need to introduce the concepts of boundary and boundary operator. The boundary of a k -simplex $\sigma = \langle p_0, \dots, p_k \rangle$ can be viewed as its geometric boundary, which is the sum of all its $(k-1)$ -faces, given by:

$$\partial_k \sigma = \sum_{i=0}^k (-1)^i \langle p_0, \dots, \hat{p}_i, \dots, p_k \rangle = \sum_{i=0}^k \langle p_0, \dots, \hat{p}_i, \dots, p_k \rangle, \quad (6)$$

where \hat{p}_i indicates that the vertex p_i is omitted. The operator ∂_k is called the boundary operator. Then the boundary of a k -chain $\mathbf{c} = \sum_j \gamma_j \sigma_j$ (σ_j is k -simplex) is the linear combination of boundaries of its k -simplices

$$\partial_k \mathbf{c} = \sum_j \gamma_j \partial_k \sigma_j, \quad \gamma_j \in \mathbb{Z}_2. \quad (7)$$

The boundary operator ∂_k maps a k -chain group C_k to a $(k-1)$ -chain group C_{k-1} . It induces the corresponding group homomorphisms, and the kernels and images of these homomorphisms can be used to construct quotient groups. Furthermore, each quotient group provides a means to distinguish two special types of chains: k -cycles and k -boundaries. For clarity, we give the definition of the kernel and image of the homomorphism ∂_k

$$\begin{aligned} \text{Ker}(\partial_k) &:= \{\mathbf{c} \in C_k \mid \partial_k \mathbf{c} = 0\}, \\ \text{Im}(\partial_k) &:= \{\partial_k \mathbf{c} \mid \mathbf{c} \in C_k\}. \end{aligned} \quad (8)$$

A k -cycle is a k -chain with empty boundary, i.e., $\partial_k \mathbf{c} = 0$. The kernel $\text{Ker}(\partial_k)$ is composed of all k -cycles and is a subgroup of C_k , denoted by Z_k . A k -boundary \mathbf{c} is a k -chain which is the boundary of a $(k+1)$ -chain \mathbf{a} , i.e., $\mathbf{c} = \partial \mathbf{a}$. Similarly, all k -boundaries form a subgroup $B_k = \text{Im}(\partial_{k+1})$ of the chain group C_k . According to the fundamental property for the homology procedure: For all integers k and every $(k+1)$ -chain \mathbf{a} , we have $\partial_k \partial_{k+1} \mathbf{a} = 0$. Therefore, we know that a k -boundary is necessarily a k -cycle. In other words, a k -boundary group B_k is a subgroup of the k -cycle group Z_k . But the reverse does not

hold, i.e., a k -cycle is not necessarily a k -boundary. To distinguish those non-boundary k -cycles, the notion of homology group is a powerful tool as follows: The k -th homology group of the object X is defined by the quotient $H_k(X) = Z_k(X)/B_k(X)$, whose element is a collection of k -chains obtained by adding k -boundaries from B_k to a given k -cycle, $\mathbf{c} + B_k$ with $\mathbf{c} \in Z_k$. We call $\mathbf{c} + B_k$ a class of H_k and use \mathbf{c} as the representative of this class. It is evident that the groups Z_k , B_k , and H_k are linear spaces, as their coefficients are taken from the binary field \mathbb{Z}_2 . The ranks of these homology group are given by the base 2 logarithm of their cardinalities, specifically:

$$\text{rank}(H_k) = \log_2(\text{card}(H_k)).$$

The rank of the k -homology group, $\text{rank}(H_k)$, is called the k -Betti number of Z_k . And we have the relation $\text{rank}(H_k) = \text{rank}(Z_k) - \text{rank}(B_k)$. The k -Betti number measures the number of k -dimensional holes of the complex X .

Homology groups provide a static characterization of the topology of a simplicial complex. For a specific r , the topology of X can be analyzed using homology tools. However, we often need to investigate the topological changes that occur as the object X varies with r . It is evident that the homology group alone cannot capture these dynamic topological changes. When the evolution of X follows a certain law, we can use persistent homology to record the persistence of specific homology classes during this process. Filtration is introduced to describe this law, resulting in a sequence of subcomplexes of the simplicial complex X

$$\emptyset = X_{r_0} \subseteq X_{r_1} \subseteq \cdots \subseteq X_{r_n} = X.$$

In practical scenarios, our emphasis is not on the specific value of r , but rather on the state itself. Therefore, the filtration is denoted as

$$\emptyset = X_0 \subseteq X_1 \subseteq \cdots \subseteq X_n = X. \quad (9)$$

The corresponding sequence of sets $\{\mathbf{c}_0, \dots, \mathbf{c}_{n-1}\}$ with the property that $X_{j+1} = X_j \cup \mathbf{c}_j$ for $j = 0, \dots, n-1$ is called a filter. A complex X with a filtration is called a filtered complex, denoted by \mathcal{X} . By definition, for a simplex $\sigma \in X_i$, it holds that $\sigma \in X_j$ for $j = i, \dots, n$. The birth time $b(\sigma)$ of a simplex σ in the filtration is defined as the smallest index i such that $\sigma \in X_j$ if and only if $j \geq b(\sigma)$. We use the simple elliptic curve $y^2 = x^3 - x$ (Figure 1(left)), where $x \in [-1, 2]$, as an example to illustrate the concept of filtration. Some samples are collected along the curve and a complex is constructed using these samples, as shown in Figure 1. We sort these points in ascending order of their function values and index them as the set $Z = \{1, 2, 3, 4, 5, 6\}$. The simplicial complex consists of $\{\langle 1 \rangle, \langle 2 \rangle, \langle 3 \rangle, \langle 2, 3 \rangle, \langle 4 \rangle, \langle 3, 4 \rangle, \langle 2, 4 \rangle, \langle 5 \rangle, \langle 1, 5 \rangle, \langle 6 \rangle, \langle 5, 6 \rangle\}$. These points naturally introduce a filter of the complex as $\mathbf{c}_0 = \langle 1 \rangle$, $\mathbf{c}_1 = \langle 2 \rangle$, $\mathbf{c}_2 = \langle 3 \rangle$, $\mathbf{c}_3 = \langle 2, 3 \rangle$, $\mathbf{c}_4 = \langle 4 \rangle$, $\mathbf{c}_5 = \langle 3, 4 \rangle$, $\mathbf{c}_6 = \langle 2, 4 \rangle$, $\mathbf{c}_7 = \langle 5 \rangle$, $\mathbf{c}_8 = \langle 1, 5 \rangle$, $\mathbf{c}_9 = \langle 6 \rangle$, $\mathbf{c}_{10} = \langle 5, 6 \rangle$. The corresponding filtration is given by $X_{j+1} = X_j \cup \mathbf{c}_j$, $j = 0, \dots, 10$.

It is important to note that different filtrations exist for some complexes. The commonly used filtrations include the Vietoris-Rips complex, Čech complex, sublevel filtration, lower-star filtration, and others [7, 14, 16, 24, 31, 48]. We here state the concept of lower star filtration (see [47, 48]). For a set U of vertices in X , its star is defined as the set of simplices that have at least one vertex in U , and its link as the set of faces of simplices

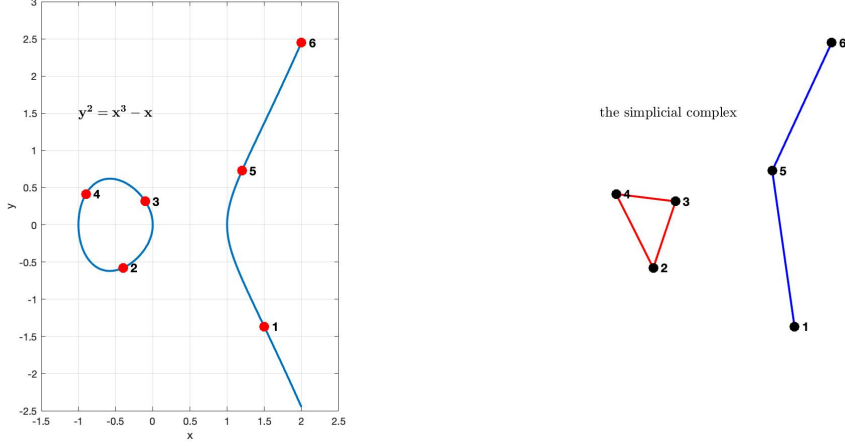


Figure 1: Elliptic curve (left) and a complex is constructed with the triangulation (right).

in the star that do not also belong the star [47, 48]:

$$\begin{aligned} \text{St } U &= \{\sigma \in X \mid \exists p \in U, p \in \sigma\}, \\ \text{Lk } U &= \{\tau \in X \mid \tau \subseteq \sigma \in \text{St } U, \tau \notin \text{St } U\}. \end{aligned} \quad (10)$$

If we endow the vertices p in X with real values $h(p)$ from a function h , the vertices can be sorted along with their neighboring vertices in the star according to these values. We assume that h is a defined and non-degenerate function for all vertices p of the given complex X , meaning that the function values are distinct for all vertices [17, 19, 47]. For the complex constructed from the elliptic curve in Fig. 1, where vertices are sorted by ascending y -coordinates, we obtain that $\text{St}\{2, 5\} = \{\langle 2 \rangle, \langle 2, 3 \rangle, \langle 2, 4 \rangle, \langle 5 \rangle, \langle 1, 5 \rangle, \langle 5, 6 \rangle\}$, $\text{St}\{4\} = \{\langle 4 \rangle, \langle 2, 4 \rangle, \langle 3, 4 \rangle\}$. The corresponding links are given by $\text{Lk}\{2, 5\} = \{\langle 3 \rangle, \langle 4 \rangle, \langle 1 \rangle, \langle 6 \rangle\}$, $\text{Lk}\{4\} = \{\langle 2 \rangle, \langle 3 \rangle\}$ respectively. Following [47, 48], we use this function to define the lower star and the lower link of p ,

$$\begin{aligned} \text{St}_- p &:= \{\sigma \in \text{St } p \mid v \in \sigma \Rightarrow h(v) \leq h(p)\}, \\ \text{Lk}_- p &:= \{\sigma \in \text{Lk } p \mid v \in \sigma \Rightarrow h(v) \leq h(p)\}. \end{aligned} \quad (11)$$

Then the sequence of subcomplexes $\{\text{St}_- p_0, \dots, \text{St}_- p_m\}$ generates a filter that forms a filtration that is called lower star filtration of h . Returning to Fig. 1, we construct the lower star filtration induced by the function y

$$\begin{aligned} X_0 &= \emptyset, X_1 = \{\langle 1 \rangle\}, X_2 = \{\langle 1 \rangle, \langle 2 \rangle\}, X_3 = \{\langle 1 \rangle, \langle 2 \rangle, \langle 3 \rangle, \langle 2, 3 \rangle\}, \\ X_4 &= \{\langle 1 \rangle, \langle 2 \rangle, \langle 3 \rangle, \langle 2, 3 \rangle, \langle 4 \rangle, \langle 2, 4 \rangle, \langle 3, 4 \rangle\}, \\ X_5 &= \{\langle 1 \rangle, \langle 2 \rangle, \langle 3 \rangle, \langle 2, 3 \rangle, \langle 4 \rangle, \langle 2, 4 \rangle, \langle 3, 4 \rangle, \langle 5 \rangle, \langle 1, 5 \rangle\}, \\ X_6 &= \{\langle 1 \rangle, \langle 2 \rangle, \langle 3 \rangle, \langle 2, 3 \rangle, \langle 4 \rangle, \langle 2, 4 \rangle, \langle 3, 4 \rangle, \langle 5 \rangle, \langle 1, 5 \rangle, \langle 6 \rangle, \langle 5, 6 \rangle\}. \end{aligned} \quad (12)$$

By examining the corresponding homology groups at each stage in this filtration, we can describe how long certain properties (classes) of the complex survive in the sequence. Typically, more emphasis is placed on how the number of homology classes (the Betti number) changes during the filtration, rather than on the exact structure of each homology group. Thus, examining a k -simplex that creates a new class alongside

a $(k + 1)$ -simplex that eliminates an existing class is sufficient to comprehend the topological changes. The core process involves tracking the moments when a new homology class emerges (is ‘born’) and when it becomes trivial or merges with another class. For a specific homology class, the birth time, denoted as b , and the death time, denoted as d , define its lifespan. We can use so-called persistence diagrams to illustrate the persistence of each k -dimensional hole. We display the persistence diagram corresponding to (12) in Fig. 2.

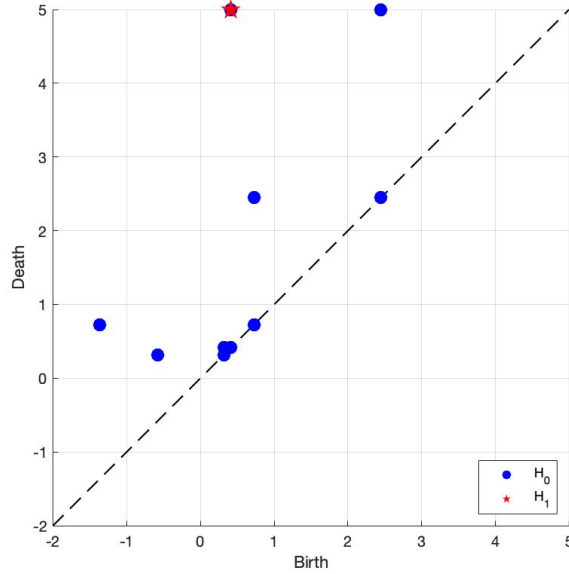


Figure 2: The persistence diagram corresponding the filtration (12).

In order to capture the variation of the Betti numbers of the homology groups at each stage of a given filtration, we assume that the filtration of X is complete. This means that each subcomplex X_{i+1} in the filtration is formed from X_i by adding exactly one simplex σ_i . The k -Betti number of a k -homology group increases by 1 when a new k -homology class is created, which occurs when a k -simplex σ_i with a certain property is added to the filtration. Such a simplex σ_i is referred to as positive. Conversely, the k -Betti number of the k -homology group decreases by 1 when a $(k + 1)$ -simplex with a specific property (referred to as negative) is added to the filtration, which destroys a k -homology class. We can analyze these properties by examining how the new simplex is connected to the preceding subcomplexes. For a given k -homology class that is created by a positive k -simplex at a certain stage r_i of the filtration and is destroyed by a $(k + 1)$ -simplex at a later stage r_j of the filtration, the corresponding k -simplex and the $(k + 1)$ -simplex can be ‘‘paired’’. Their birth time difference in the filtration is called their persistence. The pair is called persistence pair. A formal algorithm for the pairing of simplices is described in [18, 47] (See Algorithm 1).

Using the lower star filtration, it is also possible to pair the vertices. When both simplices of a pair lie in the same lower star, we call such a pair trivial. In this case, when using the (non-complete) lower star filtration, the corresponding cycle is created and destroyed simultaneously as the lower star set of the vertex is added to the filtration. This means that the existence of this class cannot be detected within the current ‘‘resolution’’ of the lower star filtration. As a result, we focus only on the nontrivial pairs, i.e., the

Algorithm 1 Pairing of simplices:

```
1: Input:  $X_i$  and  $\sigma_i$ , for  $i = 1, \dots, n$ .
2: Initialize:  $C = \emptyset$ ,  $P_k = \emptyset$ , for all possible  $k$ .
3: for  $j = 1, \dots, n$  do
4:   if  $\sigma_j$  with  $\dim \sigma_j = k$  is positive and creates the cycle  $c_j$ ,
5:   then add  $c_j$  into  $C$ , i.e.,  $C = C \cup c_j$ .
6:   elseif  $\sigma_j$  with  $\dim \sigma_j = k + 1$  is negative and  $\sigma_j$  destroys  $c_{i_0}$  in  $C$ ,
7:   then form the pair  $(c_{i_0}, c_j)$  and add this pair into  $P_k$ .
8:   end if
9:   Output:  $P_k$  (as a multiset) of persistence pairs of dimension  $k$  in the given
   filtration.
10: end for
```

nonlocal pairs (see Definition 2.1). In the following, we will pair vertices instead of simplices and use $P(X)$ to denote the collection of all pairs of vertices in X .

Definition 2.1. Assume that (σ, τ) is a pair of simplices given by Algorithm 1, where $\sigma \in \text{St } \sigma_s$ and $\tau \in \text{St } \sigma_t$. We say that σ and τ are locally paired if $s = t$ and they are non-locally paired if $s \neq t$.

Definition 2.2. Let (σ, τ) be a non-locally paired simplex pair, where $\sigma \in \text{St}_- \sigma_s$ and $\tau \in \text{St}_- \sigma_t$. We define the corresponding persistence pair of vertices as (s, t) .

3 The TV-Gaussian and PH-Gaussian priors

We describe the TV-Gaussian and PH-Gaussian priors in this section. It should be pointed out here that the space $L^\infty(\Omega)$ is not separable, and its dual space has a relatively complex structure [15]. For simplicity, we embed the admissible set K to $L^2(\Omega)$.

We begin by introducing the Gaussian measure on $L^2(\Omega)$, which serves as our reference measure. For every $\iota \in L^2(\Omega)^*$, if $\mu_0 \circ \iota^{-1}$ is a Gaussian measure on \mathbb{R} , then μ_0 is defined as a Gaussian measure on $L^2(\Omega)$. The covariance operator C_0 associated with μ_0 is given by:

$$C_0(\iota_1, \iota_2) = \int_{L^2(\Omega)} \iota_1(q) \iota_2(q) d\mu_0(q) - \mathbb{E}[\iota_1] \mathbb{E}[\iota_2], \quad \iota_1, \iota_2 \in L^2(\Omega)^*, \quad (13)$$

where $\mathbb{E}[\iota]$ denotes the mean of μ_0 , defined as:

$$\mathbb{E}[\iota] = \int_{L^2(\Omega)} \iota(q) d\mu_0(q), \quad \text{for every } \iota \in L^2(\Omega)^*. \quad (14)$$

Next we interpret (13) in a more intuitive manner and express the covariance operator differently. According to the Hahn-Banach theorem, we know that $\iota(q)$ serves, to some extent, as a means of extracting the coordinate of q . This implies that $C_0(\iota_1, \iota_2)$ represents the covariance between different coordinates, ι_1, ι_2 , of q . By the Riesz representation theorem, we no longer distinguish between $L^2(\Omega)$ and its dual $L^2(\Omega)^*$ in the following. Let $\{\varphi_n\}_{n=1}^\infty$ be an orthonormal basis of $L^2(\Omega)$. The Fourier expansion of q is given by $q(x) = \sum_{n=1}^\infty q_n \varphi_n(x)$. As taking ι as φ_i, φ_j , it gets the coordinates q_i, q_j of q by $\iota(q)$.

It can be seen that the mean and covariance operators are bounded linear and bilinear functional respectively. The bounded bilinear functional determines a bounded linear operator as follows:

$$C_0(\iota_1, \iota_2) = \langle C_0 \iota_1, \iota_2 \rangle, \quad (15)$$

where the same notation is used for both the bilinear functional and the operator. In the present paper, we consider two commonly used forms of C_0 . The first is to define the covariance operator C_0 as an integral operator with a mean squared exponential kernel:

$$C_0^{\text{exp}} \iota = \int_{\Omega} \exp\left(-\frac{|x-y|^2}{2l^2}\right) \iota(y) dy, \quad (16)$$

where $l > 0$ is a length-scale parameter. We usually use the periodic version of C_0^{exp} in some case of periodic structure, i.e., the periodic mean squared exponential kernel covariance operator C_0^{per}

$$C_0^{\text{per}} \iota = \int_{\Omega} \exp\left(-\frac{2 \sin^2(\pi|x-y|/p)}{l^2}\right) \iota(y) dy, \quad (17)$$

where $l > 0$ is a length-scale parameter and $p > 0$ is a periodicity parameter. The second is to define

$$C_0^{-\Delta} = (-\Delta)^{-s}, \quad s > 0 \quad (18)$$

with Dirichlet boundary conditions. Note that C_0 is symmetric positive and of trace class. The range of $C_0^{\frac{1}{2}}$

$$E = \left\{ q = C_0^{\frac{1}{2}} w \mid w \in L^2(\Omega) \right\} \subset L^2(\Omega),$$

which is a Hilbert space equipped with inner product [40]

$$\langle \cdot, \cdot \rangle_E = \langle C_0^{-\frac{1}{2}} \cdot, C_0^{-\frac{1}{2}} \cdot \rangle_{L^2(\Omega)},$$

is called the Cameron-Martin space of measure μ_0 .

In this paper, our goal is to estimate the unknown $q \in K$ from measured data u^η . The exact u is related to q via the forward model (1) and the data u^η is collected by (3). For convenience, we assume that the data is collected at some discrete points uniformly distributed in the domain Ω and denote the forward model as

$$u^\eta(x_i) = G(q)(x_i) + \eta(x_i), \quad x_i \in \Omega, \quad i = 1, 2, \dots, m, \quad (19)$$

where $G : K \rightarrow \mathbb{R}^m$ and η is an m -dimensional zero mean Gaussian noise with covariance matrix Σ . Under this assumption, we have the likelihood function, i.e., the distribution of u^η conditional on q is

$$\pi(u^\eta | q) \propto \exp(-\Phi(q; u^\eta)), \quad (20)$$

where

$$\Phi(q; u^\eta) := \frac{1}{2} \|G(q) - u^\eta\|_{\Sigma}^2 = \frac{1}{2} \|\Sigma^{-1/2} (G(q) - u^\eta)\|_2^2, \quad (21)$$

is often referred to as the data fidelity term in deterministic inverse problems. The Bayesian approach provides decision making under uncertainty, while the prior distribution gives additional information about uncertainty. Here we assume that the prior measure of q is μ_{pr} , and the posterior measure μ_{post} is given by the Radon-Nikodym derivative:

$$\frac{d\mu_{\text{post}}}{d\mu_{\text{pr}}}(q) = \frac{1}{Z} \exp(-\Phi(q; u^\eta)), \quad (22)$$

where Z is a normalization constant.

The Gaussian prior, $\mu_{\text{pr}} = \mu_0$, where $\mu_0 = N(0, C_0)$, is the most commonly used prior in Bayesian inverse problems. In practical terms, such a prior reflects the assumption that the unknown parameter q has a zero mean, with the covariance C_0 encoding our beliefs about the uncertainty or spread of q . Gaussian priors with covariance operators, as described in equations (16)-(18), promote smoothness by incorporating prior information that encourages regularity in the underlying function. Functions sampled from these priors are typically smooth, with continuous derivatives when using the squared exponential kernel. For the fractional Laplacian, these priors produce even smoother functions with higher regularity, particularly when using the Karhunen-Loève (KL) expansion, which can only be applied in a truncated form. However, non-smooth unknown functions q often arise in practical scenarios, such as in the infinite potential well model in the Schrödinger equation. In such cases, Gaussian priors may struggle to capture the non-smooth characteristics of the function. To address this limitation, we introduce an additional constraint for the unknown function q within the framework of the Gaussian prior. This results in a hybrid prior form, which combines the strengths of both the probabilistic Gaussian framework and regularization techniques. The concept of hybrid priors originates from the work of Z. Yao et al. [46], who proposed a more flexible prior that incorporates both uncertainty modeling and total variation methods. This hybrid approach enhances the modeling capabilities in complex systems, where both uncertainty and structural information are critical for accurate representation.

We first review the work of Yao et al. [46]. Rather than simply setting $\mu_{\text{pr}} = \mu_0$, the prior measure is defined as

$$\frac{d\mu_{\text{pr}}}{d\mu_0}(q) \propto \exp(-R(q)),$$

where $R(q)$ incorporates additional information beyond the Gaussian prior. Under this assumption, it immediately follows that the Radon-Nikodym derivative of μ_{post} with respect to μ_0 is given by

$$\frac{d\mu_{\text{post}}}{d\mu_0}(q) \propto \exp(-\Phi(q; u^\eta) - R(q)) := \exp(-V(q)), \quad (23)$$

which recovers the standard formulation with Gaussian priors. Let the sample space be the Sobolev space $H^1(\Omega)$, defined as follows:

$$H^1(\Omega) = \{q \in L^2(\Omega) \mid \partial_x^\alpha q \in L^2(\Omega) \text{ for all } |\alpha| \leq 1\},$$

where $\alpha = (\alpha_1, \alpha_2, \dots, \alpha_5)$ and $|\alpha| = \sum_{i=1}^5 \alpha_i$, and the associated norm is

$$\|q\|_{H^1} = \sum_{|\alpha| \leq 1} \|\partial_x^\alpha q\|_{L^2(\Omega)}.$$

The regularization term is chosen to be the TV seminorm [46]

$$R_{\text{TV}}(q) = \lambda \|q\|_{\text{TV}} = \lambda \int_{\Omega} |\nabla q| dx, \quad (24)$$

where λ is a prescribed positive constant. Moreover, the posterior can be written as

$$\frac{d\mu_{\text{post}}}{d\mu_0} = \exp(-\Phi(q; u^\eta) - R_{\text{TV}}(q)). \quad (25)$$

We next introduce a novel hybrid prior that combines the strengths of Gaussian distributions with topological information, creating a more refined and informative framework for settings where the underlying structure is crucial. This approach blends the uncertainty modeling of Gaussian priors, which provide a probabilistic framework with a known covariance structure, with topological insights that capture the shape, connectivity, and features of the parameter space. By integrating these components, we achieve a prior that reflects both the variability in the data and the inherent structural constraints of the system.

The proposed prior term is based on the concept of persistence distance, as formulated using persistence pairs in [47], and can be viewed as a generalization of the total variation (TV) prior. To better understand the relationship, we consider the triangulation of the graph of the unknown function q . This triangulation forms a simplicial complex, denoted by Q , which is homeomorphic to the graph of q . Additionally, we interpret the triangulation as a linear spline approximation of q on some partition I with knots $\{x_i\}_{i=0}^m$. The simplicial complex Q , together with the lower star filtration of Q , is denoted as \mathcal{Q} , providing a topological structure for the prior.

3.1 1-d case

First, we consider the case of 1-dimensional function. We denote the spline approximation by q , i.e., q is a piecewise linear function with $q(x_i) = q(x_i)$ and denote the space of linear splines with the partition I by $S_1(I)$. We need to introduce the concept of persistence distance based on persistence pairs and the corresponding difference of function values of q . The persistence distance consists of a sum of distances of function values of q being local extrema of the function q . It can be proven that the persistence distance is closely related to the discrete total variation of q . Compared to the discrete total variation, the persistence distance contains more information about the topological structure of the function [47].

In computational topology, barcodes and persistence diagrams are the popular visualization tools to display the persistence pairs. Each persistence pair (x_k, x_l) corresponds to the point $(q(x_k), q(x_l))$ in the persistence diagram, and the distance of this point to the diagonal line $y = x$, given by $|q(x_k) - q(x_l)|$, reflects the “topological significance” of the pair, which gives us some information about the “topological relevance” of these two local extrema of q . Important features correspond to points being further away from the diagonal, i.e., to persistence pairs (x_k, x_l) with significant distances $|q(x_k) - q(x_l)|$. We denote the set of persistence pairs of q by P_+ . When considering the sequence $\{-q(x_j)\}_{j=0}^m$, we can obtain a second set P_- of persistence pairs for $-q$ on I . It can be seen that P_+ and P_- partially coincide, but usually are not equal. When persistence pairs occur twice, i.e.,

when they are included in $P_+ \cup P_-$, the corresponding absolute differences of function values are counted twice. A set in which an element can appear multiple times is referred to as a multiset. And the boundary extremum knots x_0 and x_{\max} are contained in at most one persistence pair, either in one from P_+ or in one from P_- , since they are not regarded when being a local maximum knot. Indeed, x_0 (resp. x_{\max}) will not occur in any persistence pair, i.e., neither in P_+ nor in P_- , if it is a global extremum knot.

Definition 3.1. [47] For a given piecewise linear spline function $q \in S_1(I)$, we define the persistence distance by

$$\|q\|_{\text{per}} = \sum_{(x_k, x_l) \in P_+} |q(x_l) - q(x_k)| + \sum_{(x_k, x_l) \in P_-} |q(x_l) - q(x_k)|,$$

i.e., as the sum over all distances of function values for the persistence pairs in P_+ and P_- .

The persistence distance is neither a metric, nor a semi-norm. It conveys substantial information about the structure of a function $q \in S_1(I)$ and is closely related to the discrete total variation $\text{TV}(q)$. It can be proven that the following theorem holds [47].

Theorem 3.1. [47] Let I be a partition of Ω . Then for each function $q \in S_1(I)$, we have

$$\|q\|_{\text{per}} + \max_{x, \tilde{x} \in I} |q(x) - q(\tilde{x})| = \text{TV}(q),$$

where $\text{TV}(q)$ is the discrete total variation of q defined by

$$\text{TV}(q) := \sum_{j=0}^{m-1} |q(x_{j+1}) - q(x_j)|.$$

In contrast to the total variation $\text{TV}(q)$, the persistence distance is defined as the sum of differences in function values at local extrema of q , thereby capturing the function's topological characteristics. Small values of $|q(x) - q(\tilde{x})|$, which arise from closely paired extrema (x, \tilde{x}) , are typically indicative of high-frequency oscillations or noise. On the other hand, large values of $|q(x) - q(\tilde{x})|$ correspond to prominent structural features of the function q . Let for simplicity

$$P(q) = P_+ \cup P_- \cup \{(x, \tilde{x})\}$$

be the set of all (persistence) pairs, where (x, \tilde{x}) denotes the pair of knots whose corresponding function values are the global minimum and the global maximum of q . For the one-dimensional case, we define the prior as

$$\frac{d\mu_{\text{pr}}}{d\mu_0}(q) \propto \exp \left(- \sum_{(x_j, \tilde{x}_j) \in P(q)} \alpha_j(q) |q(x_j) - q(\tilde{x}_j)| \right), \quad (26)$$

where $\alpha_j = \alpha_j(q) = \alpha(q, x_j, \tilde{x}_j)$ depends on the persistence $|q(x_j) - q(\tilde{x}_j)|$. This corresponds to taking the regularization term $R_{1d}(q)$ as

$$R_{1d}(q) = \sum_{(x_j, \tilde{x}_j) \in P(q)} \alpha_j(q) |q(x_j) - q(\tilde{x}_j)|. \quad (27)$$

The parameter α_j should be large for small distances $|\mathbf{q}(x_j) - \mathbf{q}(\tilde{x}_j)|$, emphasizing the penalization of minor oscillations or noise. Conversely, α_j should be relatively small for large distances $|\mathbf{q}(x_j) - \mathbf{q}(\tilde{x}_j)|$, allowing significant features of the function \mathbf{q} to be preserved. In [47], the weight strategy is proposed to deal with denoising problems

$$\alpha_j(\mathbf{q}) = (\kappa_j + 1)\theta \frac{1}{1 + \beta|\mathbf{q}(\tilde{x}_j) - \mathbf{q}(x_j)|}, \quad (28)$$

where $\beta > 0$ and $\kappa_j = \kappa(x_j, \tilde{x}_j)$ is the order of the pair (x_j, \tilde{x}_j) in its chain of pairs and $\theta > 1$. If we take $\alpha_j \equiv \lambda$ for all j (with λ given in (24)), the proposed prior reduces to the TV prior. In this sense, we say that it is a generalization of the total variation (TV) prior.

3.2 2-d case

The concept of the 1-dimensional persistence prior can be extended to the 2-dimensional case. We only consider the case where Ω is a square domain. In this case, q can be viewed as an image. The values of q on vertices of the triangulation are arranged in a matrix. We denote this matrix as $\mathbf{Q} = [\mathbf{Q}_{ij}]$, $i = 1, \dots, I$, $j = 1, \dots, J$, the i -th row as \mathbf{Q}^i , and the j -th column as \mathbf{Q}_j . The rows and columns of \mathbf{Q} are then processed in a manner similar to the 1-dimensional case. We treat each row (resp. column) as a vertex set of some 1-d spline function. To simplify the notation, we use \mathbf{q}^i and \mathbf{q}_j to denote the linear spline function with knot values \mathbf{Q}^i and \mathbf{Q}_j respectively. Then we impose a PH prior on each row (resp. column) and sum them, i.e., we take

$$R_{2d}(q) = \sum_{i=1}^I R_{1d}(\mathbf{q}^i) + \sum_{j=1}^J R_{1d}(\mathbf{q}_j), \quad (29)$$

and set

$$\frac{d\mu_{\text{pr}}}{d\mu_0}(q) \propto \exp(-R_{2d}(q)). \quad (30)$$

This approach is equivalent to monitoring the topological structure of slices of the two-dimensional function along each direction. Although it cannot fully capture the topological information of the entire 2D function, it still provides valuable insights by preserving key topological features along specific slices.

If we denote both R_{1d} and R_{2d} by R_{PH} , the posterior can be written as

$$\frac{d\mu_{\text{post}}}{d\mu_0} = \exp(-\Phi(q; u^\eta) - R_{\text{PH}}(q)). \quad (31)$$

4 The pCN sampling algorithm

Several widely-used MCMC sampling methods can be derived through discretization of Langevin-type stochastic differential equations (SDEs) [12, 13]. Consider the following SDE:

$$\frac{dq}{d\tau} = -K(\gamma DV(q) + Lq) + \sqrt{2K} \frac{dW}{d\tau}, \quad (32)$$

where $K = C_0$ or I (identity operator), $\gamma = 0$ or 1 , $L = C_0^{-1}$ is the precision operator for the Gaussian measure μ_0 , DV denotes the Fréchet derivative of V , W represents a standard Brownian motion in $L^2(\Omega)$. This SDE preserves the prior measure μ_0 as its invariant distribution when $\gamma = 0$ and the posterior measure μ_{post} when $\gamma = 1$. This fundamental property provides the theoretical foundation for constructing MCMC samplers via temporal discretization of the continuous-time dynamics. Among various discretization schemes, the preconditioned Crank-Nicolson (pCN) method (see Algorithm 2) has emerged as a particularly effective approach for equations of type (32), especially when $K = C_0$. The pCN discretization takes the following semi-implicit form:

$$q_{n+1} - q_n = -\frac{\Delta\tau}{2}C_0(DV(q_n) + DV(q_{n+1})) - \frac{\Delta\tau}{2}(q_n + q_{n+1}) + \sqrt{2\Delta\tau C_0}\xi_n, \quad (33)$$

where $\xi_n \sim \mathcal{N}(0, I)$ is Gaussian white noise. An approximate semi-implicit scheme can be written as:

$$\left(1 + \frac{\Delta\tau}{2}\right)q_{n+1} = -\Delta\tau C_0 DV(q_n) + \left(1 - \frac{\Delta\tau}{2}\right)q_n + \sqrt{2\Delta\tau C_0}\xi_n. \quad (34)$$

For sufficiently small $\Delta\tau$, we obtain a first-order approximation by neglecting higher-order terms ($o(\sqrt{\Delta\tau})$):

$$q_{n+1} = \left(1 + \frac{\Delta\tau}{2}\right)^{-1} \left(1 - \frac{\Delta\tau}{2}\right)q_n + \left(1 + \frac{\Delta\tau}{2}\right)^{-1} \sqrt{2\Delta\tau C_0}\xi_n. \quad (35)$$

By introducing the parameter $\rho \approx \sqrt{2\Delta\tau}$ and recognizing that $\xi := C_0^{1/2}\xi_n \sim \mu_0$, we arrive at the standard pCN proposal:

$$\hat{q} = \sqrt{1 - \rho^2}q_n + \rho\xi, \quad (36)$$

where $\xi \sim \mu_0$. This proposal exactly preserves the Gaussian prior μ_0 . The Metropolis-Hastings acceptance step then incorporates the likelihood to ensure convergence to the posterior μ_{post} . Clearly, this method circumvents the need to compute complex derivatives, thereby facilitating its application to the sampling process in this study.

Algorithm 2

- 1: **Initialization:** Set sample number N and $q^{(0)} = 0$. Compute the corresponding negative log likelihood function $\Phi(q^{(0)}; u^\eta)$ and regularization term $R(q^{(0)})$. Denote

$$\varphi^{(0)} := \Phi(q^{(0)}; u^\eta) + R(q^{(0)}).$$

- 2: Move the sample to a proposal $\hat{q}^{(n)} = \sqrt{1 - \rho^2}q^{(n-1)} + \rho\xi$, where $\xi \sim \mu_0$.
- 3: Compute the negative log likelihood function $\Phi(\hat{q}^{(n)}; u^\eta)$ and regularization term $R(\hat{q}^{(n)})$. Denote

$$\hat{\varphi}^{(n)} := \Phi(\hat{q}^{(n)}; u^\eta) + R(\hat{q}^{(n)}).$$

- 4: Compute the accept probability $\alpha = \min\{1, \exp[\hat{\varphi}^{(n)} - \varphi^{(n-1)}]\}$.
 - 5: Set $q^{(n)} = \hat{q}^{(n)}$ if $\alpha > r$, else $q^{(n)} = q^{(n-1)}$, where r is a uniform random number on $[0, 1]$.
 - 6: When $n < N$, implement step 2 - step 5.
-

5 Numerical tests

In this section, we present numerical experiments to validate the effectiveness of the proposed prior. We compare the performance of three different priors: the standard Gaussian prior, the TV-Gaussian prior, and our proposed TP-Gaussian prior. The results demonstrate the advantages of our approach in terms of accuracy and robustness.

In all numerical tests, the data is generated by adding a 1‰ relative error to the numerical solution using the exact q , i.e.,

$$u^\eta(x_o) = u(q)(x_o) + \eta(x_o), \quad \eta = 1\text{‰}\|u(q)\|\xi, \quad (37)$$

where $u(q)$ is the numerical solution and $\xi \sim N(0, I)$ and x_o is observational points uniformly distributed in Ω . And the error between the samples and the exact solution q is computed by

$$\|q^{(n)} - q\| = \frac{1}{\sqrt{m-1}} \left(\sum_{i=1}^m |q^{(n)}(x_i)^2 - q(x_i)^2| \right)^{\frac{1}{2}}, \quad (38)$$

where $\{x_i\}$ are the space discretized mesh points. We employ the pCN algorithm (see Algorithm 2) to generate posterior samples from the target distribution [46]. To ensure convergence to the stationary distribution and mitigate the effects of initial transients, we incorporate a burn-in phase and apply thinning (lag) to reduce sample autocorrelation. Specifically, we discard the first half of the generated samples as burn-in and set a lag of 5 between retained samples. The sample mean is then computed from the remaining samples to estimate the parameter q .

5.1 1d case

Example 1. First, we consider a smooth 1-dimensional function in $\Omega = (0, 1)$

$$q(x) = 1 + x(1-x)\sin(4\pi x).$$

We generate $N = 10^5$ samples following Algorithm 2. In this experiment, we compare the effectiveness of different priors introduced in Section 3: the Gaussian priors with $C_0^{-\Delta}$ (with $s = 1.5$) and the periodic mean exponential kernel C_0^{per} , as well as the TV-Gaussian prior and the PH-Gaussian prior.

For the latter two priors, we use the periodic mean squared exponential kernel Gaussian in μ_0 as the reference measure. The parameters for these priors are set as follows: $l = 1.0$, $p = 1$ for C_0^{per} , and $\theta = 3$, $\beta = 0.001$ in the PH prior as given in (28).

The weight parameter λ in both the TV-Gaussian and PH-Gaussian priors is set to 4. The proposal parameter ρ in Algorithm 2 is set to 0.002. Numerical reconstructions are presented in Fig. 3 (see Example 1), demonstrating that the proposed prior is well-suited for smooth scenarios. From the results shown, it is evident that the PH-Gaussian prior performs competitively compared to the other priors.

Example 2. In the second example, we consider the exact q as a 1-dimensional piecewise constant function on $\Omega = (0, 1)$:

$$q(x) = \begin{cases} 1.5, & \frac{1}{3} \leq x < \frac{2}{3}, \\ 0.5, & \text{otherwise.} \end{cases}$$

This numerical experiment demonstrates the performance of both the baseline prior from Example 1 and the proposed prior μ_0 with the kernel $C_0^{-\Delta}$ (with parameter $s = 1.6$). For consistency with Example 1, we explicitly list only the modified parameters: the length scale $l = 0.2$ in C_0^{per} , the regularization weight $\lambda = 20$, and the proposal step size $\rho = 0.01$. The numerical comparison is given in Fig. 3. Obviously, when dealing with a function that has jumps, using only a Gaussian prior leads to unsatisfactory results. Specifically, the Gaussian prior μ_0 with $C_0^{-\Delta}$ enforces an excessively high degree of smoothness on the function due to its highly smooth eigenfunctions within the domain. This makes it difficult to capture local features, especially for non-smooth functions. Whether using the Karhunen-Loève expansion, finite difference methods, or finite element methods to discretize the covariance operator $C_0^{-\Delta}$, we encounter the problem that either the number of expansion terms becomes too large, or the discretization grid is limited by machine precision, preventing the capture of local features. When using μ_0 with C_0^{per} , the result exhibits oscillations, likely arising from the properties of the periodic exponential covariance kernel, particularly its inherent smoothness and long-range dependencies, which can introduce oscillatory artifacts into the solution. In contrast, the TV-Gaussian and PH-Gaussian priors can significantly alleviate these issues. In the subsequent examples, we will no longer employ μ_0 with the covariance operator $C_0^{-\Delta}$, as our focus is solely on testing non-smooth scenarios.

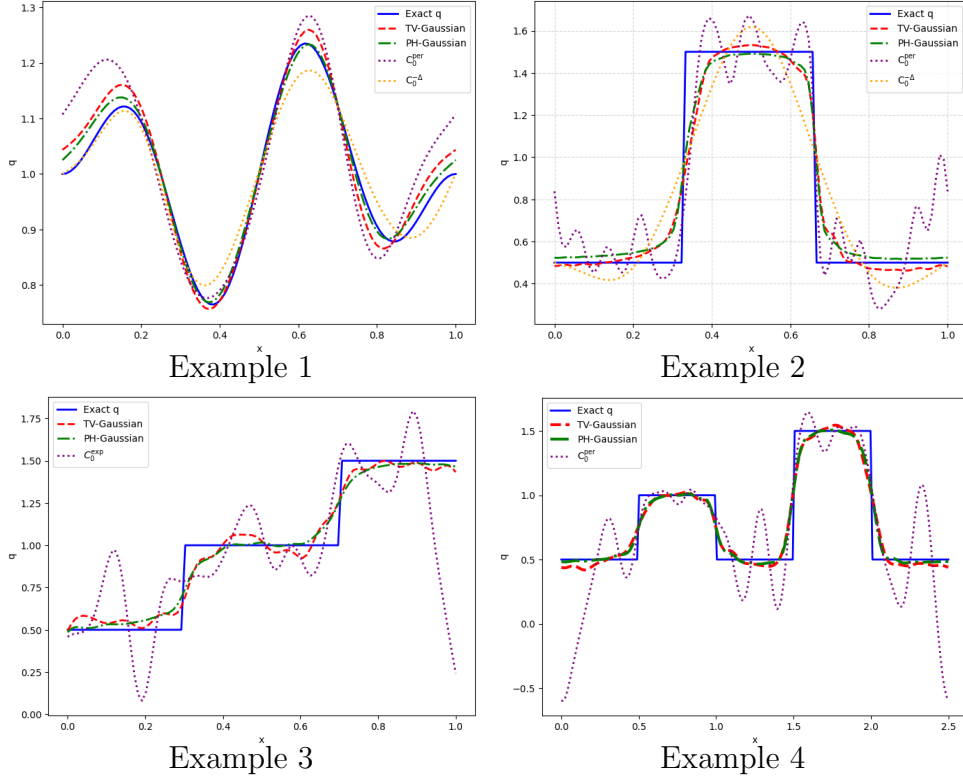


Figure 3: Numerical comparisons using different priors for 1d case.

Example 3. We test the proposed prior on a 1D step function,

$$q(x) = \begin{cases} 0.5, & 0 \leq x < 0.3, \\ 1, & 0.3 \leq x < 0.7, \\ 1.5, & 0.7 \leq x \leq 1. \end{cases}$$

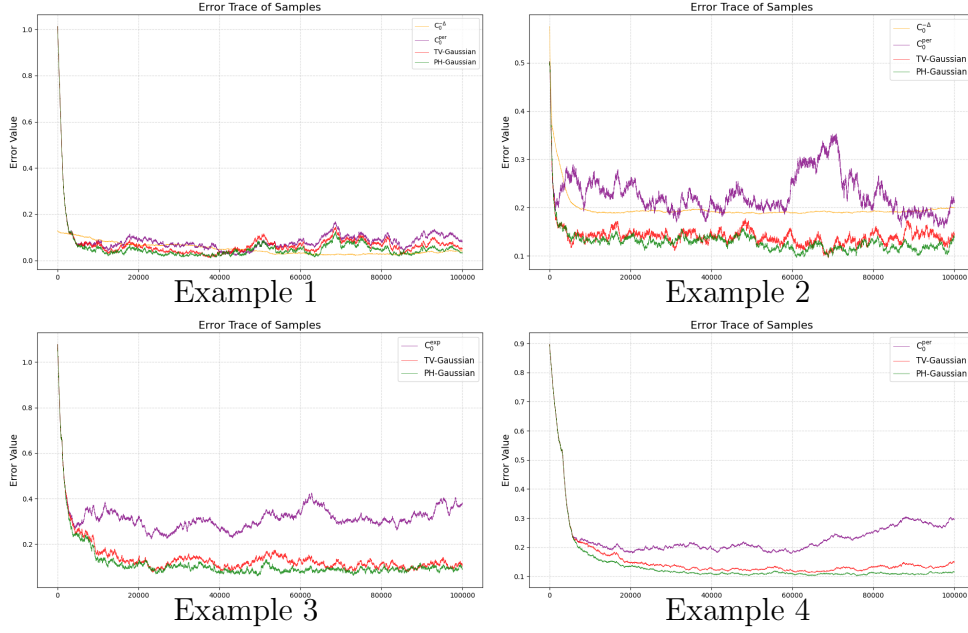


Figure 4: The error traces for Example 1-4.

In this example, the Gaussian measure μ_0 with C_0^{exp} is used as the base measure in the Gaussian, TV-Gaussian, and PH-Gaussian priors. The parameter l is set to 0.05 in all cases. The weight parameter λ is set to 10, and the Markov transition parameter β is set to 0.005. Other parameters are chosen to be the same as in Example 2. The numerical results are displayed in Fig. 3. As in Example 2, the oscillation occurs when using the prior μ_0 with the exponential covariance kernel and the reason is similar to that in Example 2. In addition, the TV-Gaussian and PH-Gaussian priors can fulfill the case well.

Example 4. We adjust the piecewise constant in Example 2 to a more complicated case as

$$q(x) = \begin{cases} 0.5, & 0 \leq x < 0.5, \\ 1, & 0.5 \leq x < 1.0, \\ 0.5, & 1.0 \leq x \leq 1.5, \\ 1.5, & 1.5 \leq x < 2.0, \\ 0.5, & 2.0 \leq x \leq 2.5. \end{cases}$$

We still use the periodic mean squared exponential kernel Gauss as the base measure with $l = 0.2$, $p = 2.5$. The weight parameter $\lambda = 20$. The parameter of the PH-Gaussian prior $\theta = 3$ and $\beta = 0.001$ in (28). We generate 2×10^5 samples by Algorithm 2. From the displayed results (see Fig. 3), it is evident that the same phenomenon observed in Examples 2 and 3 is replicated here.

Example 5. In this example, we consider a function that is derived from the Weierstrass function

$$W(x) = \sum_{n=0}^{\infty} a^n \cos(b^n \pi x),$$

where $0 < a < 1$, b is a positive odd integer and $ab > 1 + \frac{3\pi}{2}$. By $W_K(x)$ we denote the truncated series to the first $K + 1$ terms. Take the exact q as $q(x) = \frac{2}{\pi} \arctan(W_K(x)) + 1$ with $a = 0.4$, $b = 4$ and $K = 10$. Here, we do not adhere to the strict parameter rule in the Weierstrass function. In the sampling process, we apply a transform $q(x) = \exp(g(x))$ and treat g as the unknown target. As in Example 3, the mean squared exponential kernel Gaussian is used as the base measure. We set $l = 0.01$ and the weight parameter $\lambda = 5$. This test reveals that the oscillatory limitations of the squared exponential kernel prior are exacerbated, whereas our approach still achieves robust performance (see Fig. 5). It should be noted that we cannot assert the numerical performance of the PH-Gaussian prior is superior to that of the TV-Gaussian prior based solely on this example. The differences observed in Fig. 5 are partly influenced by the parameter settings, particularly the weight parameter λ . However, when the weight parameter λ is held constant, the PH-Gaussian prior yields more robust results compared to the TV-Gaussian prior. In the regularization framework, the weight parameter acts as the regularization parameter, which is both crucial and challenging to select. Consequently, the PH-Gaussian prior offers a more flexible and adaptable algorithm.

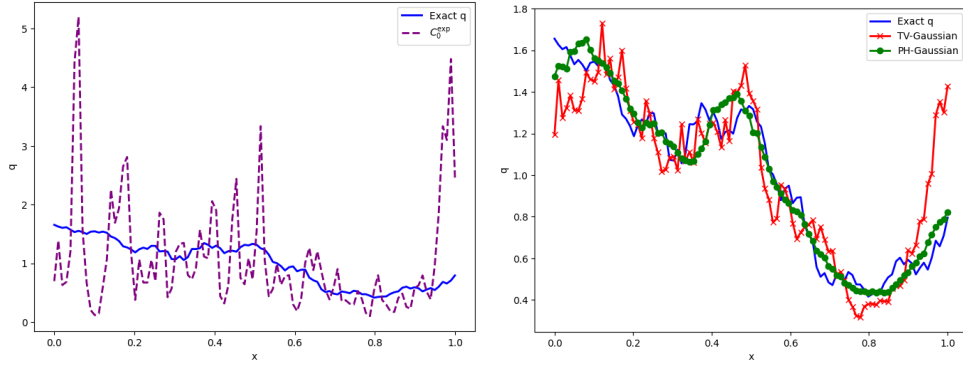


Figure 5: Numerical comparisons using different priors for Example 5.

We plot the error traces in Fig. 4, with the error computed according to (38). These results demonstrate that the proposed prior delivers strong numerical performance, particularly for functions with discontinuities. While the PH and TV priors yield comparable results in most cases, a discernible difference emerges in Example 5 when applied to a highly oscillatory function—here, the advantage of our method becomes visually apparent.

5.2 2d case

Example 6. We consider a 2d piecewise constant function in a squared domain $\Omega = (0, 1) \times (0, 1)$

$$q(x, y) = \begin{cases} 1.5, & (x - 0.5)^2 + (y - 0.5)^2 \leq 0.25^2, \\ 0.5, & \text{otherwise.} \end{cases}$$

In this example, we take $\mu_0 = N(0, C_0^{\text{exp}})$ with the parameter $l = 0.1$. We generate $N = 40,000$ samples. The weight parameter λ in the TV-Gaussian and TP-Gaussian priors is set to 2. Other parameters remain the same as those in Example 1.

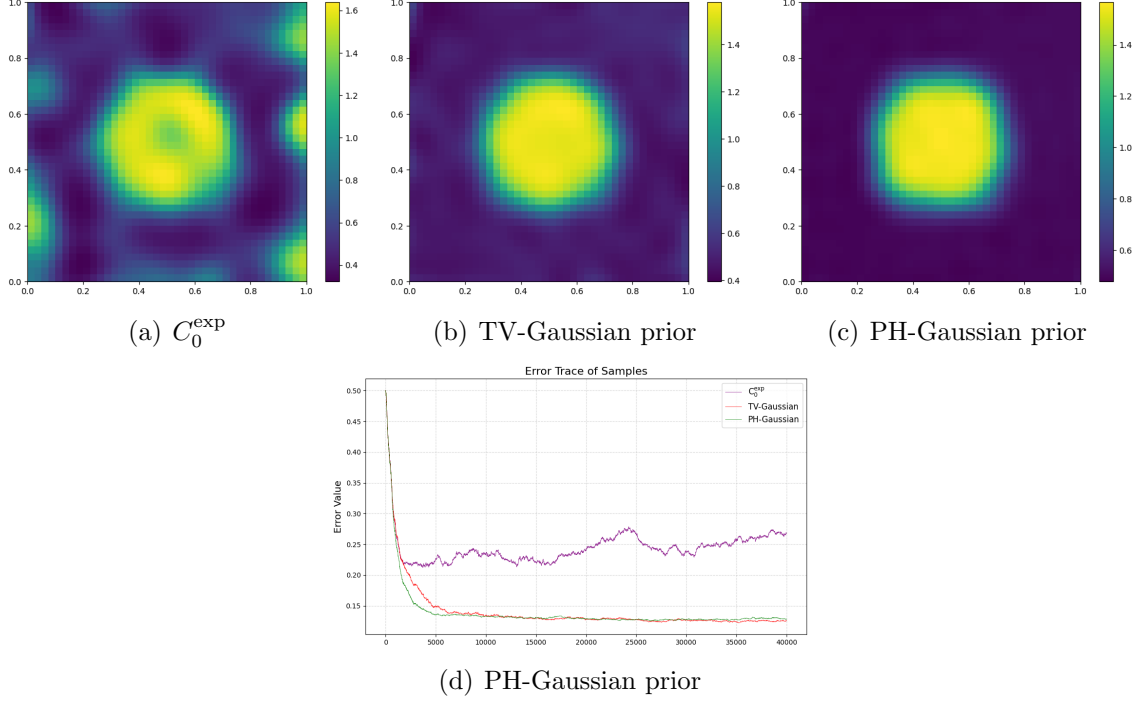


Figure 6: Numerical illustration using different priors for Example 6: (a) the Gaussian prior with C_0^{exp} ; (b) the TV-Gaussian prior; (c) the PH-Gaussian prior; (d) the error trace.

Example 7. We consider a 2d piecewise constant function in a squared domain $\Omega = (0, 2) \times (0, 2)$

$$q(x, y) = \begin{cases} 1, & (x - 0.6)^2 + (y - 0.6)^2 \leq 0.3^2, \\ 1.5, & (x - 1.4)^2 + (y - 1.4)^2 \leq 0.3^2 \\ 0.5, & \text{otherwise.} \end{cases}$$

In this example, apart from adjusting the parameter l to 0.1 and λ to 5, all other parameters remain the same as in Example 5. We generate $N = 8,000$ samples.

From the 2D examples, we observe conclusions nearly identical to those in the 1D case. This confirms that the PH-Gaussian prior yields reliable reconstruction results, performing competitively with the TV-Gaussian prior and outperforming the standard Gaussian prior alone. The error trace plots further demonstrate that the PH-Gaussian prior exhibits superior numerical effectiveness compared to the TV-Gaussian prior when reconstructing functions with complex topological structures, as evidenced in Example 5.

6 Conclusion

We employ persistent homology as a tool to construct a hybrid prior for estimating the unknown variable in the inverse potential problem within the Bayesian framework. A key feature of this prior is that it constrains the topological variation of the unknown variable, effectively imposing a regularity condition akin to the total variation (TV). Moreover, the PH-based prior is defined on a topological space, which is a mild limitation. This

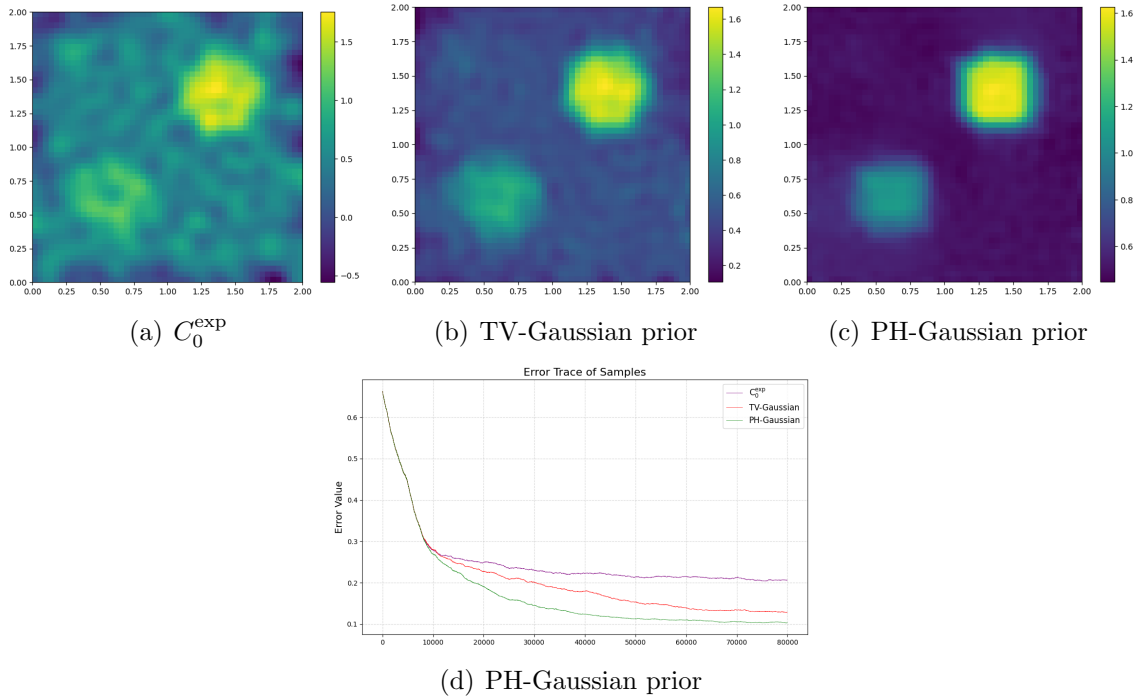


Figure 7: Numerical illustration using different priors for Example 7: (a) the Gaussian prior with C_0^{exp} ; (b) the TV-Gaussian prior; (c) the PH-Gaussian prior; (d) the error trace.

flexibility allows the method to be easily extended to a broader range of applications. In numerical practice, the PH-Gaussian prior demonstrates excellent performance. Its ability to produce robust results is enhanced by the flexibility of its parameter settings, which allow for more adaptable and precise tuning.

References

- [1] G. Bal and G. Uhlmann. Inverse diffusion theory of photoacoustics. *Inverse Problems*, 26(085010):20pp, 2010.
- [2] J. M. Bardsley. Gaussian Markov random field priors for inverse problems. *Inverse Problems and Imaging*, 7(2):397–416, 2013.
- [3] L. Baudouin and A. Mercado. An inverse problem for Schrödinger equations with discontinuous main coefficient. *Applicable Analysis*, 87(10-11):1145–1165, 2008.
- [4] L. Baudouin and J. Puel. Uniqueness and stability in an inverse problem for the Schrödinger equation. *Inverse Problems*, 18:1537–1554, 2002.
- [5] M. Benning and M. Burger. Modern regularization methods for inverse problems. *Acta Numerica*, pages 1–111, 2018.
- [6] A. Beskos, M. Girolami, S. Lan, P. Farrell, and A. Stuart. Geometric MCMC for infinite-dimensional inverse problems. *J. Comput. Phys*, 335:327–351, 2017.

- [7] Jean-Daniel Boissonnat, Frédéric Chazal, and Mariette Yvinec. *Geometric and Topological Inference*. Cambridge University Press, 2018.
- [8] T. Bui-Thanh and O. Ghattas. An analysis of infinite dimensional Bayesian inverse shape acoustic scattering and its numerical approximation. *SIAM/ASA Journal on Uncertainty Quantification*, 2(1), 2014.
- [9] A. Carpio, E. Cebrian, and A. Gutierrez. Object based Bayesian full-waveform inversion for shear elastography. *Inverse Problems*, 39(075007):28pp, 2023.
- [10] A. Carpio, S. Iakunin, and G. Stadler. Bayesian approach to inverse scattering with topological priors. *Inverse Problems*, 36(105001):29pp, 2020.
- [11] M. Choulli. Some stability inequalities for hybrid inverse problems. *Comptes Rendus. Mathématique*, 359(10):1251–1265, 2021.
- [12] S. L. Cotter, G. O. Roberts, A. M. Stuart, and D. White. MCMC methods for functions: modifying old algorithms to make them faster. *Statistical Science*, 28(3):424–446, 2013.
- [13] M. Dashti and A. Stuart. *The Bayesian Approach to Inverse Problems*. Springer, 2017.
- [14] T. Dey and Y. Wang. *Computational Topology for Data Analysis*. Cambridge University Press, 2022.
- [15] N. Dunford and J. T. Schwartz. *Linear Operators, Part I: General Theory*, volume VII. John Wiley & Sons, 1988.
- [16] H. Edelsbrunner and J. Harer. *Computational Topology: An Introduction*. the American Mathematical Society, 2010.
- [17] H. Edelsbrunner, J. Harer, and A. Zomorodian. Hierarchical Morse complexes for piecewise linear 2-manifolds. *Discrete Comput. Geom.*, (30):87–107, 2003.
- [18] H. Edelsbrunner, D. Letscher, and A. Zomorodian. Topological persistence and simplification. *Discrete Comput. Geom.*, 28:511–533, 2002.
- [19] H. Edelsbrunner, D. Morozov, and V. Pascucci. Persistence-sensitive simplification of functions on 2-manifolds. In *SCG '06 Proceedings of the Twenty-Second Annual Symposium on Computational Geometry*, pages 127–134, 2005.
- [20] H. W. Engl, K. Kunisch, and A. Neubauer. Convergence rates for Tikhonov regularization of nonlinear ill-posed problems. *Inverse Problems*, 5:523–540, 1989.
- [21] H. W. Engl, K. Kunisch, and A. Neubauer. *Regularization of Inverse Problems*. Kluwer, 1996.
- [22] T. Furuya, P. Kow, and J. Wang. Consistency of the Bayes method for the inverse scattering problem. *Inverse Problems*, 40(055001):24pp, 2024.
- [23] M. Giordano and R. Nickl. Consistency of Bayesian inference with Gaussian process priors in an elliptic inverse problem. *Inverse Problems*, 36(085001):35pp, 2020.

- [24] A. Hatcher. *Algebraic Topology*. Cornell Department of Mathematics, <http://www.math.cornell.edu/~hatcher>, 2001.
- [25] J. Huang, Z. Deng, and L. Xu. A Bayesian level set method for an inverse medium scattering problem in acoustics. *Inverse Problems and Imaging*, 15(5):1077–1097, 2021.
- [26] M. A. Iglesias, K. Lin, and A. M. Stuart. Well-posed Bayesian geometric inverse problems arising in subsurface flow. *Inverse Problems*, 30(114001):39pp, 2014.
- [27] M. A. Iglesias, Y. Lu, and A. M. Stuart. A Bayesian level set method for geometric inverse problems. *Interface and Free Boundaries*, 18:181–217, 2016.
- [28] K. Ito and B. Jin. *Inverse Problems: Tikhonov Theory and Algorithms*. Hackensack, NJ: World Scientific, 2015.
- [29] B. Jin, X. Lu, Q. Quan, and Z. Zhou. Convergence rate analysis of Galerkin approximation of inverse potential problem. *Inverse Problems*, 39(015008):26, 2023.
- [30] B. Jin, Q. Quan, and W. Zhang. Stochastic convergence analysis of inverse potential problem. <https://arxiv.org/html/2410.14106v2>, 2025.
- [31] T. Kaczynski, K. Mischaikow, and M. Mrozek. *Computational Homology*. Springer-Verlag New York, 2004.
- [32] J. P. Kaipio, T. Huttunen, T. Luostari, T. Lähivaara, and P. B. Monk. A Bayesian approach to improving the Born approximation for inverse scattering with high-contrast materials. *Inverse Problems*, 35(084001):19pp, 2019.
- [33] J. P. Kaipio and E. Somersalo. *Statistical and Computational Inverse Problems*, volume 160. Springer, 1 edition, 2005.
- [34] J. Latz. On the well-posedness of Bayesian inverse problems. *SIAM/ASA Journal on Uncertainty Quantification*, 8(1):451–482, 2020.
- [35] J. Latz. Bayesian inverse problems are usually well-posed. *SIAM Review*, 65(3):831–865, 2023.
- [36] Z. Li, Z. Deng, and J. Sun. Extended-sampling-Bayesian method for limited aperture inverse scattering problems. *SIAM Journal on Imaging Sciences*, 13(1):422–444, 2020.
- [37] R. Nickl. Bernstein-von Mises theorems for statistical inverse problems I: Schrödinger equation. *J. Eur. Math. Soc.*, 22(8):2697–2750, 2020.
- [38] R. Nickl, S. van de Geer, and S. Wang. Convergence rates for penalized least squares estimators in PDE constrained regression problems. *SIAM Journal on Uncertainty Quantification*, 8(1):374–413, 2020.
- [39] H. H. Pennes. Analysis of tissue and arterial blood temperatures in the resting human forearm. *J. Appl. Physiol.*, 1:93–122, 1948.
- [40] G. Da Prato. *An Introduction to Infinite-Dimensional Analysis*. Berlin: Springer, 2006.

- [41] A. M. Stuart. Inverse problems: A Bayesian perspective. *Acta Numerica*, 19:451–559, 2010.
- [42] J. Tarantola. *Inverse Problem Theory and Methods for Model Parameter Estimation*. SIAM, 2005.
- [43] D. Trucu, D. B. Ingham, and D. Lesnic. Space-dependent perfusion coefficient identification in the transient bio-heat equation. *J. Engrg. Math.*, 67:307–315, 2010.
- [44] Z. Wang, J. M. Bardsley, A. Solonen, T. Cui, and Y. M. Marzouk. Bayesian inverse problems with l_1 priors: A randomize-then-optimize approach. *SIAM Journal on Scientific Computing*, 39(5), 2017.
- [45] M. Yamamoto and J. Zou. Simultaneous reconstruction of the initial temperature and heat radiative coefficient. *Inverse Problems*, 17:1181–1202, 2001.
- [46] Z. Yao, Z. Hu, and J. Li. A TV-Gaussian prior for infinite-dimensional Bayesian inverse problems and its numerical implementations. *Inverse Problems*, 32(7):075006, 2016.
- [47] Y. Zheng. *Application of Persistent Homology in Signal and Image Denoising*. PhD thesis, Georg-August-Universität Göttingen, 2015.
- [48] Afra J. Zomorodian. *Topology for Computing*. Cambridge University Press, 2005.